The Astronomical Journal, 155:117 (9pp), 2018 March https://doi.org/10.3847/1538-3881/aaa6d6

A New Dark Vortex on Neptune

Michael H. Wong[1,11], Joshua Tollefson[1,12], Andrew I. Hsu[1,13], Imke de Pater[1,11,12], Amy A. Simon[2], Ricardo Hueso[3], Agustín Sánchez-Lavega[3], Lawrence Sromovsky[4], Patrick Fry[4], Statia Luszcz-Cook[5], Heidi Hammel[6], Marc Delcroix[7], Katherine de Kleer[8], Glenn S. Orton[9], and Christoph Baranec[10]
[1] University of California, Berkeley, CA 94720, USA; mikewong@astro.berkeley.edu
[2] NASA Goddard Space Flight Center, 8800 Greenbelt Road, Greenbelt, MD 20771, USA
[3] Universidad del Pais Vasco Bilbao, Spain
[4] University of Wisconsin, Madison, WI 53706, USA
[5] American Museum of Natural History and Columbia University, New York NY, USA
[6] Association of Universities for Research in Astronomy, Washington DC 20004-1752, USA
[7] Societe Astronomique de France, France
[8] California Institute of Technology Pasadena CA 91109, USA
[9] Jet Propulsion Laboratory, 4800 Oak Grove Drive, California Institute of Technology, Pasadena, CA, USA
[10] Institute for Astronomy, University of Hawai'i at Mānoa, Hilo, HI 96720-2700, USA
Received 2017 November 21; revised 2017 December 22; accepted 2017 December 29; published 2018 February 15

Abstract

An outburst of cloud activity on Neptune in 2015 led to speculation about whether the clouds were convective in nature, a wave phenomenon, or bright companions to an unseen dark vortex (similar to the Great Dark Spot studied in detail by *Voyager 2*). The *Hubble Space Telescope* (*HST*) finally answered this question by discovering a new dark vortex at 45 degrees south planetographic latitude, named SDS-2015 for "southern dark spot discovered in 2015." SDS-2015 is only the fifth dark vortex ever seen on Neptune. In this paper, we report on imaging of SDS-2015 using *HST*'s Wide Field Camera 3 across four epochs: 2015 September, 2016 May, 2016 October, and 2017 October. We find that the size of SDS-2015 did not exceed 20 degrees of longitude, more than a factor of two smaller than the *Voyager* dark spots, but only slightly smaller than previous northern-hemisphere dark spots. A slow (1.7–2.5 deg/year) poleward drift was observed for the vortex. Properties of SDS-2015 and its surroundings suggest that the meridional wind shear may be twice as strong at the deep level of the vortex as it is at the level of cloud-tracked winds. Over the 2015–2017 period, the dark spot's contrast weakened from about −7% to about −3%, while companion clouds shifted from offset to centered, a similar evolution to some historical dark spots. The properties and evolution of SDS-2015 highlight the diversity of Neptune's dark spots and the need for faster cadence dark spot observations in the future.

Key words: astrometry – hydrodynamics – planets and satellites: atmospheres – planets and satellites: gaseous planets – planets and satellites: individual (Neptune) – techniques: high angular resolution

1. Introduction

Voyager 2 provided the first high-resolution glimpse of Neptune in 1989, observing two dark spots. We assume these features are anticyclonic vortices based on their behavior (Smith et al. 1989), although there has never been an actual measurement of their internal circulation. Since *Voyager*, only Hubble has discovered dark vortices: two in the 1990s, and one in 2015 (Table 1). Ground-based facilities lack the resolution to detect these low-contrast features at blue optical wavelengths, while infrared observations do not detect the dark spots themselves, only their bright companion features. This is not quite the case for Uranus, where we have seen dark features at red wavelengths in Hubble images (Hammel et al. 2009) and at near-IR wavelengths in Keck H-filter images (Sromovsky et al. 2015). The five Neptune dark spots exhibited surprising diversity, in terms of size, shape, companion cloud distribution, oscillatory behavior, meridional drift rates, and meandering. Neptune's dark vortices come and go on much shorter timescales compared to similar anticyclones on Jupiter, which evolve over decades (e.g., Ingersoll et al. 2007; Shetty & Marcus 2010; Simon et al. 2014). Many questions remain as to how dark vortices originate, what controls their drift and oscillation, how they interact with the environment, and how they eventually dissipate. Vortex behavior also provides insight into the structure and dynamics of the surrounding atmosphere.

The discovery of SDS-2015 was enabled by the annual cadence of the Outer Planet Atmospheres Legacy (OPAL) program, which acquires maps covering two consecutive rotations of each giant planet, annually. The Neptune observations are part of OPAL's large time-domain survey of atmospheric evolution (Simon et al. 2015), which began in 2014 with observations of Uranus (Irwin et al. 2017).

Companion clouds are usually associated with dark vortices and are thought to result from ambient air being diverted upward as flow is perturbed over the vortex (Smith et al. 1989; Stratman et al. 2001). The appearance and evolution of companion clouds has been different for all of the dark vortices observed to date, with SDS-2015 (Figure 1) having persistent companions that may exhibit longitudinal oscillations in their mean position (Hueso et al. 2017). The brightness of companion clouds may be related to the vortex top altitude; a

[11] Astronomy Department.
[12] Earth and Planetary Sciences Department.
[13] Physics Department.

Table 1
Characteristics of Neptune's Dark Vortices

Name	Discovery	Demise	Latitude[a]	Size Lon. × Lat.	Meridional Drift	References
GDS	1989	1990	−20°	38° × 15°	+0.°11/day equatorward	Smith et al. (1989)
DS2	1989	<1994	−55°	39° × 6°	±2.°4 oscillation	Sromovsky et al. (1993)
NDS-1994	1994	1998–2000	+32°	35° × 10°	0°/day	Hammel et al. (1995), Sromovsky et al. (2001)
NDS-1996	1996	1997–1998	+15°	22° × 12°	0°/day	Sromovsky et al. (2001)
SDS-2015	2015	>2017	−49°	15° × 5°	−2.°5/year poleward	Wong et al. (2016)

Note. Latitude, size, and meridional drift rates are representative values. Actual values were known to vary in time, except for meridional drift of NDS-1994 and NDS-1996, which were stable in latitude. The actual demise of a dark vortex has never been observed, so values listed here are estimates (see the text). The northern spots have been renamed in this paper to establish a consistent nomenclature for post-*Voyager* dark spots.
[a] Planetographic latitude is used throughout this work.

global circulation model of the GDS (Stratman et al. 2001) found that cloud opacity weakened as the top of the vortex reached higher into the tropopause region. Their deepest model vortex had the highest companion cloud opacity.

The *Voyager* observations revealed many different types of oscillations and drifts in the behavior of dark vortices GDS and DS2 (Sromovsky et al. 1993). The center of the GDS oscillated in longitude, and also drifted slowly equatorward, with some intermittent poleward meandering. It also exhibited a "rolling" appearance, where the aspect ratio oscillated in phase with a rotation of the ellipse axes. LeBeau & Dowling (1998) modeled these oscillations and identified a common physical mechanism explaining the drift of both terrestrial hurricanes, and the GDS on Neptune. In both cases, the spinning of the vortices advects the background atmospheric potential vorticity, creating a weak dipole of vorticity aligned approximately north–south. LeBeau & Dowling (1998) postulated the destruction of these vortices, as they drift equatorward and experience either Rossby-wave radiation, or loss of material as they merge with regions of similar potential vorticity. The actual origin or dissipation of a Neptunian dark vortex has never been conclusively documented. Discovery dates are listed in Table 1 because origin dates are unknown. Likewise, the demise or dissipation of these vortices has never been precisely determined. End dates in the table are estimates based on extrapolated positions, the disappearance of bright companions, and absence in subsequent observations.

The meridional drift of vortices acts as a probe of Neptune's zonal flow, which is puzzling in many ways (Limaye & Sromovsky 1991; Sromovsky et al. 1995; Hammel & Lockwood 1997; Sromovsky et al. 2001; Fitzpatrick et al. 2014; Sánchez-Lavega et al. 2018; Tollefson et al. 2018). Neptune has a single retrograde equatorial jet with a speed of ∼400 m s^{-1}, and two prograde circumpolar jets with speeds around 250 m s^{-1}. Dispersions above 200 m s^{-1} have been measured between cloud features at the same latitude on Neptune. This observed velocity dispersion may be explained by temporal variability in the wind field, vertical wind shear, rapid evolution of cloud morphology, and/or longitudinal variability. Wave propagation, rather than mass transport, may also determine the observed motion of cloud features. Persistent, well-separated features at different latitudes have been observed to move at a common zonal rate, invisibly linked (Sromovsky et al. 2001; Martin et al. 2012). LeBeau & Dowling (1998) found that the rate of north–south drift of the vortex is very sensitive to the background potential vorticity gradient (i.e., the horizontal wind shear). Thus, measuring meridional drift may reveal fine structure in the zonal wind profile that cannot be derived by cloud-tracking, while oscillation may reveal meandering in the background jet (Karkoschka 2011).

Here, we report the size, shape, motion, and contrast of SDS-2015, based on observations spanning 2015–2017.

2. Observations

Observations reported here were taken with the UVIS detector of the WFC3 instrument aboard the *Hubble Space Telescope* (*HST*). Spectral responses of WFC3/UVIS filters listed here are given in Dressel (2016).

2.1. Cadence

Table 2 lists four epochs of observations of the dark vortex. In Figure 1, we show images and maps of Neptune at each epoch. The original discovery of SDS-2015 in OPAL data led to a supplementary Midcycle program, focusing on the blue wavelengths where the vortex itself is most evident. Only 16 days before the OPAL 2015 observations, WFC3 imaging of Neptune taken in support of VLA observations (GO-14044) barely missed the dark vortex. Companion clouds were seen, but the exposures were acquired some 20–30 minutes before SDS-2015 rotated onto the disk.

2.2. Detector Readout

We used 512 × 512 subarrays to minimize read time and instrument memory transfer overhead (buffer dumps), except for exposures using the methane-band quad filters (FQ727N, FQ619N), which generate 2K × 2K subarray frames, like all quad-filter exposures. Rather than pairing FQ727N methane-band observations with the FQ750N continuum filter, we used F763M. This filter's wider bandpass includes both continuum and CH_4-band contributions, preserving information content (and vertical resolution) while still permitting the advantageous 512 × 512 subarray readout. Although visual comparison of FQ727N and FQ750N images is more straightforward, using F763M enables more time-on-target during an *HST* orbit.

2.3. Photometric Calibration

For the FQ727N frames, we applied corrections to remove photometric errors from fringing, an effect expected to be in the 2%–5% range based on analysis of flat field data (Wong 2010). The actual magnitude of the correction across the regions of the

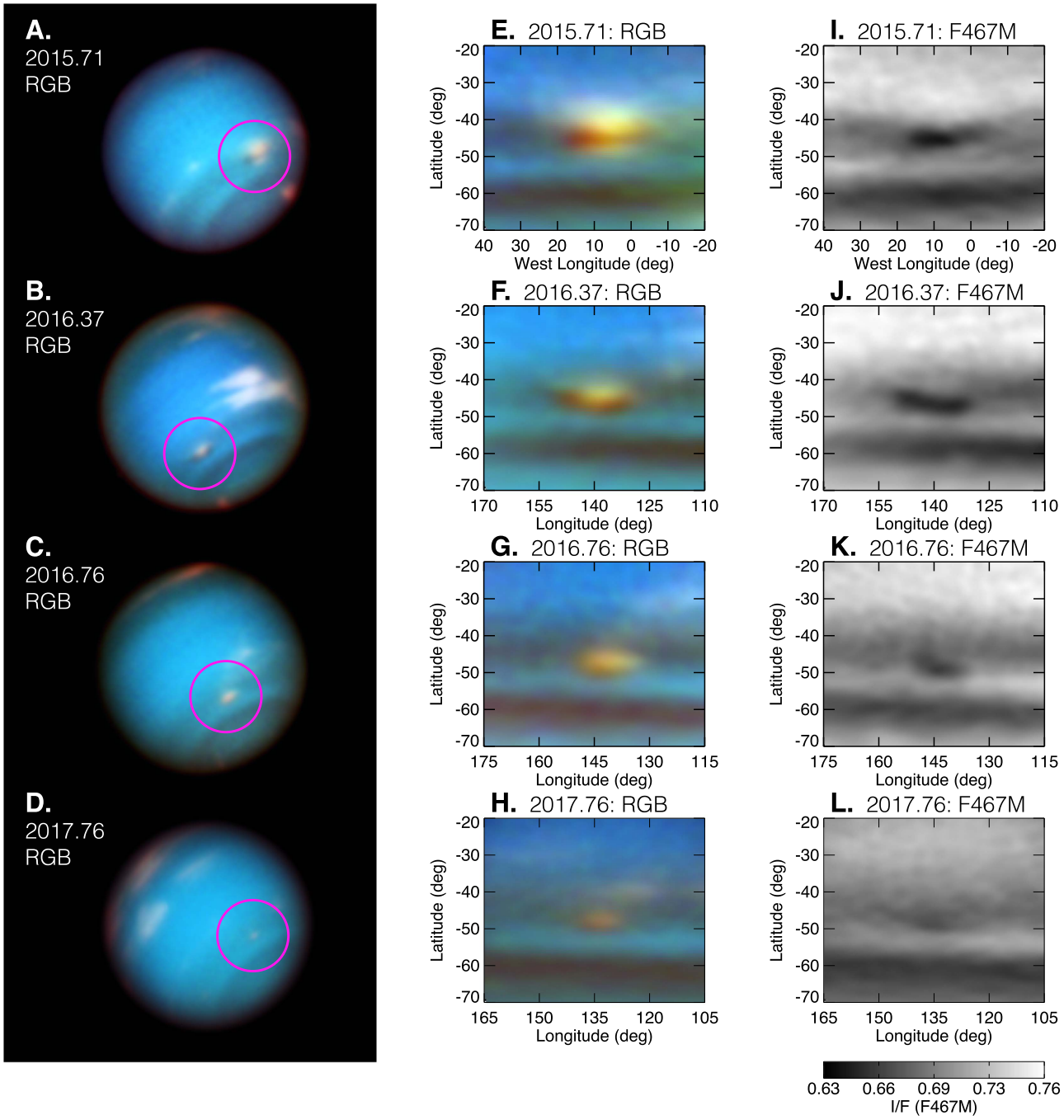

Figure 1. Gallery of SDS-2015 images and maps. [A, B, C, D] Red/green/blue (RGB) composite images at four epochs (see Table 2), co-added from multiple frames using the frydrizzle rotational dithering approach described in Section 2.5. [E, F, G, H] RGB cylindrical maps of the dark vortex at each epoch. [I, J, K, L] Blue (F467M) filter images show the dark vortex itself most clearly. The brightness scale is the same for all epochs. The F763M data (red channel in color maps) span I/F 0.08 to 0.35 on a square root stretch. The F547M data (green channel in color maps) span I/F 0.48 to 0.60 on a linear stretch. The F467M data (blue channel in color maps, greyscale in panels I–L) span I/F 0.63 to 0.76 on a linear stretch (see colorbar).

detector where Neptune was observed was 0.5%–1.5%, a smaller effect than predicted. This is because part of the overall 2%–5% fringing amplitude in this filter bandpass is corrected by the pipeline flat fields (obtained using a continuum light source), leaving just the error due to the difference in spectral energy distribution between the calibration source and Neptune's scattered solar spectrum. We also minimized the fringing amplitude by placing Neptune on an area of the detector where fringing is relatively smooth over the 50 pixel size scale of Neptune's disk. In some areas, fringing maxima/minima are separated by only 10 pixels.

In the 2015–2017 time range, the WFC3 instrument team at Space Telescope Science Institute implemented a set of significant revisions to their photometric calibration pipeline, collectively termed "UVIS 2.0." The revisions included new flat fields and normalization procedures (Mack et al. 2016), and new sensitivity values for each filter (Deustua et al. 2016, 2017). All Neptune data presented here, although acquired by *HST* prior to

Table 2
HST/WFC3 Observations of Neptune in the SDS-2015 era

Times (UTC)	Program ID	Filters (number of frames)
2015.71 (2015 Sep 18 16:48 to 2015 Sep 19 06:19)	OPAL GO-13937 (PI Simon)	F467M (4), F547M (4), F657N (4), F763M (4), F845M (8), FQ727N (4), FQ619N (4)
2016.37 (2016 May 16 03:47 to 04:16)	Midcycle GO-14492 (PI Wong)	F336W (1), F390M (1), F410M (1), F467M (6), F547M (6), F763M (3), FQ727N (2)
2016.76 (2016 Oct 03 11:04 to 2016 Oct 04 04:59)	OPAL GO-14334 (PI Simon)	F467M (4), F547M (4), F657N (4), F763M (4), F845M (8), FQ727N (4), FQ619N (4)
2017.76 (2017 Oct 06 05:49 to 2017 Oct 07 03:15)	OPAL GO-14756 (PI Simon)	F467M (8), F547M (8), F657N (8), F763M (8), F845M (16), FQ727N (8), FQ619N (8)

Note. Observing programs listed here mapped Neptune over at least one full rotation, but times listed apply only to exposures in which SDS-2015 is on the face of the disk. Additional data from program GO-14044 (PI de Pater), 2015.67, are not listed but were used for background atmosphere analyses (e.g., Table 3).

these revisions, have been recalibrated using the UVIS 2.0 photometry. The UVIS 2.0 improvements have not yet been implemented for WFC3/UVIS quad filters.

2.4. Navigation and High-level Science Products (HLSPs)

We navigated the images by aligning synthetic limb-darkened planetary disks to the data (Lii et al. 2010), giving a navigation precision of 0.0825 pixels. We estimate a navigation accuracy of about 0.18 pixels for the F467M filter images, leading to disk-center latitude/longitude uncertainties of about $0^{\circ}.3$. Global maps of Neptune acquired by the OPAL program are available as HLSPs on the MAST archive,[14] as described in Simon et al. (2015, 2016).

Navigated single-frame image data for all programs listed in Table 2 can also be obtained from MAST[15] as HLSPs ending in the extension "nav.fits." Each file is a multi-extension FITS file, similar to *HST* "drz.fits" files but with additional processing and data. The processing consists of corrections for cosmic ray hits using the LA Cosmic method (van Dokkum 2001) and for fringing in long-wavelength narrow-band filters (Wong 2011). The additional data includes FITS keywords containing target ephemeris data provided by JPL Horizons,[16] and four FITS extensions giving the planetographic latitude, west longitude, emission angle, and solar incidence angle for each pixel on the planet's disk. In addition to the STScI-supplied PHOTFLAM inverse sensitivity keyword that converts image data units from $e^{-}\ s^{-1}$ to erg $cm^{-2}\ s^{-1}\ \AA^{-1}$, we include a PHOTIF keyword that converts $e^{-}\ s^{-1}$ to planetary reflectivity units of I/F, and an associated SIG_PHOT keyword giving the photometric uncertainty in the I/F calibration.

2.5. Rotational Dithering

Relative to OPAL program observations, the midcycle program was intended to improve image quality and short-wavelength coverage, specifically focusing on the dark vortex. Short-wavelength coverage was improved by adding blue filters and dropping two longer wavelength filters, and image quality was improved by taking a larger number of frames in the blue filters. We then co-add the map data, accounting for the planet's rotation and the longitudinal drift of the dark spot.

Astronomical images of static targets can be improved by combining individual frames with drizzle methods (resampling and co-adding), which has the added benefit of being able to reject cosmic ray events and other image defects (e.g., Fruchter & Hook 2002). We would also like to co-add Neptune images, to improve sampling of the *HST*/WFC3 PSF and to average over pixels with nonuniform response, but, each exposure in our program differs due to Neptune's rotation as well as advection by atmospheric winds. In order to combine frames, additional steps must be taken, following an algorithm known informally as frydrizzle. The frydrizzle algorithm is fully described in Section 3.1 of Fry et al. (2012). The principal steps of our slightly modified procedure (we add limb-darkening treatment that was not necessary at the wavelengths used in Fry et al. 2012) are:

1. Navigate each frame to associate each element of the image data with the appropriate latitude, longitude, and emission/incidence angles.
2. Apply a limb-darkening correction to normalize reflectances to a common viewing geometry.
3. If images separated by a significant amount of time, shift (or "advect") each latitude using an a-priori zonal wind field, to correct for differential rotation.
4. Co-add data in latitude/longitude space rather than image x, y space.
5. If creating a co-added disk image on the sky (rather than co-added map in longitude-latitude space), then restore limb-darkening effects and re-map reflectances onto the globe.

3. Results

3.1. Morphology

Measurements of the size and location of SDS-2015 are based on albedo contrasts inside and outside the vortex, which appears as a 5%-level contrast feature at blue wavelengths. We estimate the boundary of the vortex to be located where the contrast reaches its half-power point, and accurate measurement of this location relies on determining the effect of limb darkening, to distinguish between the intrinsic albedo contrast of the vortex itself, and apparent contrasts due to variation in emission angle across the span of the dark spot.

[14] OPAL archive page: https://archive.stsci.edu/prepds/opal, 10.17909/T9G593.
[15] Dark vortex archive page: https://archive.stsci.edu/prepds/sds-2015, 10.17909/T9G67P.
[16] JPL Horizons server: http://ssd.jpl.nasa.gov/?horizons.

Table 3
Limb Darkening Parameters Used for Image Analysis

HST WFC3/UVIS Filter	k (global)	k (35°–55°S)
F336W	0.804 ± 0.011	0.804 ± 0.012
F390M	0.825 ± 0.005	0.807 ± 0.009
F410M	0.836 ± 0.007	0.813 ± 0.017
F467M	0.867 ± 0.016	0.823 ± 0.026
F547M	0.798 ± 0.041	0.765 ± 0.074

Note. Limb darkening is modeled using the Minnaert equation (Equation (1)). Values of k were found by linearizing image data where emission and incidence angles <75°, and uncertainties reflect scatter from instrumental noise and from actual spatial/temporal variation. Data from epochs 2015.67, 2015.71, 2016.37, and 2016.76 were used to derive limb-darkening coefficients.

We use the Minnaert equation to convert observed $I/F_{\rm obs.}$ to limb-darkening corrected $I/F_{\rm corr.}$:

$$I/F_{\rm corr.} = I/F_{\rm obs.}\,\mu_0^{-k}\mu^{(1-k)}, \quad (1)$$

where μ_0 is the cosine of the incidence angle and μ is the cosine of the emission angle. $I/F_{\rm corr.}$ can also be called the disk-center I/F, or the Minnaert albedo. This limb-darkening function was originally used to describe lunar reflectivity (Minnaert 1941). Although simple functions of this type do not perfectly capture limb-darkening behavior of Neptune's vertically and horizontally inhomogeneous atmosphere, we still use Equation (1) to achieve a first-order brightness correction, especially at emission/incidence angles less than 75°. For each wavelength, we derived the appropriate value of k by fitting to data at longitudes excluding the dark vortex. Best fit parameters based on four data sets (two in 2015 and two in 2016) are listed in Table 3.

Maps in Figure 1 show reflectivity with this first-order limb-darkening correction applied. East–west cuts through these maps are shown in Figure 2. These photometric profiles, from co-added F467M maps, were used to estimate widths and positions of SDS-2015 at the four observational epochs, with results listed in Table 4.

The largest source of uncertainty in the size and position estimates of Table 4 comes from the influence of the omnipresent companion clouds. Comparison of the RGB and F467M maps in Figure 1 consistently show reduced contrast within the vortex at locations where companion cloud opacity is high. Thus, we have defined error bars that encompass the directly observed vortex bounds (half-power points in contrast profiles like those in Figure 2) and the potentially larger size of the vortex including a qualitative compensation for vortex area masked by the companion cloud.

3.2. Contrast

The contrast of the vortex with respect to the surroundings was determined for wavelengths where the dark spot is visible, and reported in Figure 3. The contrast of the vortex in F467M has been decreasing since its discovery, with a very low contrast detected in the 2017 observations.

Contrasts were determined using the darkest location in the vortex (not necessarily the center, where companion cloud reflectivity was sometimes significant). At wavelengths longer than 547 nm, the dark spot is actually brighter than its surroundings, because the contrast is dominated by aerosols associated with the companion cloud. The relative background at the darkest location was found by linear interpolation, fitted to background levels outside the vortex. As with Sromovsky et al. (2002), we find maximum contrast in the F467M bandpass, although the SDS-2015 contrasts are consistently larger than most contrast measurements of NDS-1994 and NDS-1996 reported by Sromovsky et al. (2002).

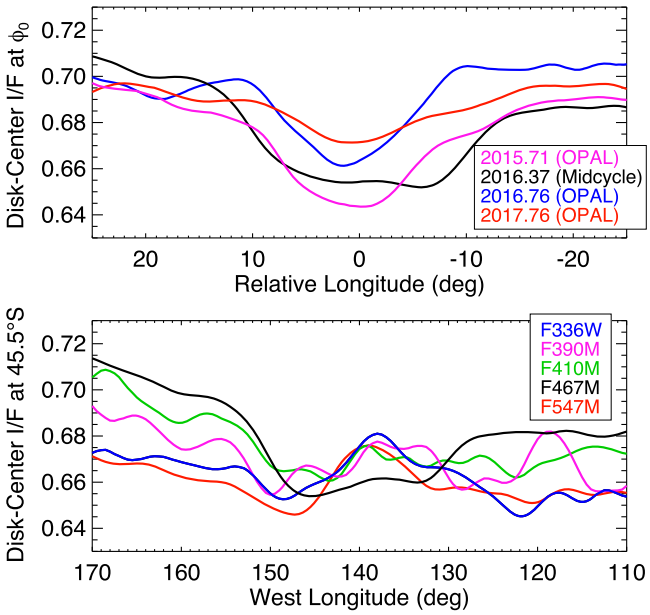

Figure 2. Photometric cuts through SDS-2015 used for size, position, and contrast measurements. Top panel: east–west cuts are shown in the highest-contrast filter (F467M) at the four epochs. Vortex center positions are as listed in Table 4. Bottom panel: east–west cuts for multiple filters are shown, for the 2016.37 epoch. The latitude of these cuts is slightly to the north of the estimated dark spot center (compare F467M trace with that in top panel, and refer to map in Figure 1(J). This was done to measure the maximum contrast at other wavelengths where the companion cloud contribution diminishes contrast at the center of the vortex. Limb darkening corrections have been applied.

3.3. Drift Rates

Over the time that SDS-2015 has been observed, it drifted polewards until it reached −49° S (Figure 4). There is no large statistical difference between two models of its meridional drift: (1) a linear poleward drift of $2.^{\circ}5$/year in 2015–2016, with no change between 2016.76 and 2017.76; or (2) a poleward drift of $1.^{\circ}7$/year over the full period of the observations. Model 1 (3-point fit) gives a drift rate very close to the change in companion cloud position of $\sim 2.^{\circ}4$/year based on all 2015 measurements in Hueso et al. (2017), specifically their Figure 19.

Longitudinal drift rates for SDS-2015 and its companion clouds are listed in Table 5. Data are derived from Hueso et al. (2017) for the entire 2015B period (2015.51–2015.95), and from OPAL data for the remaining three epochs. The 2016.37 epoch covered only a single Neptune rotation, so the temporal baseline was not long enough to measure longitudinal drifts with any certainty.

Zonal mean velocities in Table 5, from the 6th-order polynomial fit of Sromovsky et al. (1993), were measured by tracking discrete cloud features, presumably composed of CH_4, located at pressures of 1.4 bar or less (de Pater et al. 2014). Dark vortex companion clouds are also thought to be CH_4

Table 4
Morphology of SDS-2015

Epoch	Longitudinal Width ($2a$)	Latitudinal Width ($2b$)	Central Longitude (λ_0)	Central Latitude (ϕ_0)	Aspect Ratio (a/b)
2015.71	16.°8 ± 4.°0 (5120 ± 1230 km)	5.°5 ± 0.°6 (2300 ± 270 km)	9.°1 ± 1.°0	45.°6 ± 0.°2 S	2.2 ± 0.6
2016.37	19.°5 ± 1.°5 (5770 ± 440 km)	6.°4 ± 3.°8 (2690 ± 1580 km)	140.°3 ± 3.°3	46.°3 ± 1.°0 S	2.1 ± 1.3
2016.76	11.°3 ± 2.°7 (3190 ± 770 km)	5.°8 ± 3.°1 (2450 ± 1310 km)	142.°5 ± 1.°1	48.°9 ± 0.°9 S	1.3 ± 0.8
2017.76	13.°0 ± 2.°7 (3720 ± 770 km)	3.°8 ± 0.°5 (1580 ± 210 km)	134.°8 ± 0.°9	49.°0 ± 0.°2 S	2.4 ± 0.6

Note. Centers and widths are determined by measuring half-power points in brightness profiles (Figure 2 top) in the F467M data. Multiple images are combined per epoch to achieve higher signal to noise; this requires combining data after correction for limb darkening (using Equation (1) and values in Table 3). Aspect ratios are calculated using linear dimensions (km) rather than longitude/latitude. Uncertainties include the potential obscuration of part of the dark spot by the bright companion clouds (see last paragraph of Section 3.1).

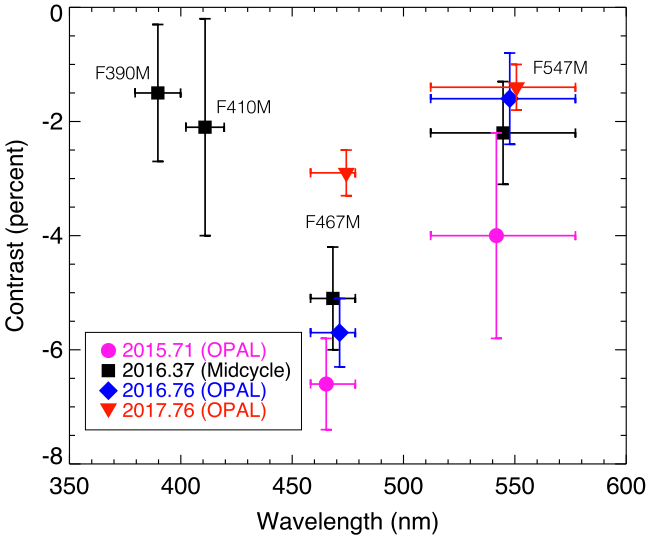

Figure 3. Spectral contrast between SDS-2015 and its surroundings. The contrast C is defined as, $C = (I/F_{DS} - I/F_{surr.})/(I/F_{surr.})$, where I/F_{DS} is defined at λ_0, ϕ_0 (see Table 4), and $I/F_{surr.}$ is a linear fit to data at longitudes well separated from the spot, at the same latitude of the vortex. Error bars include random noise, systematic photometric uncertainty, and spatial variation across the dark spot. Data points are averages of multiple frames (Table 2). Data points for F467M and F547M data are horizontally offset for clarity, but in all cases the horizontal error bars give the filter widths taken from Table 6.2 of Dressel (2016).

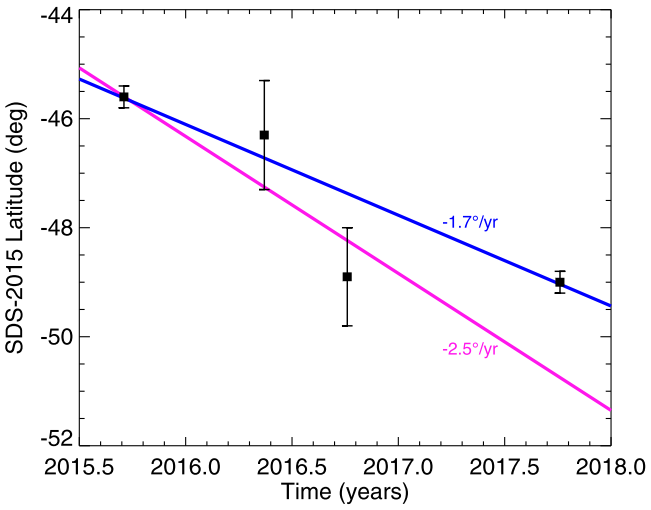

Figure 4. Poleward drift of SDS-2015. A linear drift rate of $-2.°5$/year fits SDS-2015 positions in the 2015–2016 time period (with no change in latitude between 2016.76 and 2017.76). A drift rate of $-1.°7$/year fits SDS-2015 positions over the full 2015–2017 period. Neither fit is strongly favored over the other statistically: χ^2_ν(3 points) = 1.5; χ^2_ν(4 points) = 1.6.

Table 5
Eastward Drift Rates

		Eastward Velocity (m s^{-1})		
Date	Lat. (deg)	Zonal Mean	SDS-2015	Companions
2015B	−40.1	−142	⋯	−94
2015.71	−45.6	−69	−90	⋯
	−41.0	−131	⋯	−95
2016.76	−48.9	−22	−40	⋯
	−46.5	−56	⋯	−42
2017.76	−49.0	−20	−39	⋯
	−47.5	−42	⋯	−35

Note. The first epoch of measurement, 2015B, gives the drift rate of the companion cloud determined from ground-based and *HST* observations spanning the 2015.51–2015.95 time range from Hueso et al. (2017). Other epochs are based on two consecutive Neptune rotations, as described in Table 2. The formal uncertainty of the 2015B drift rate is only 0.1 m s^{-1}, due to the long temporal baseline and high density of measurements. Uncertainties in *HST*-derived drift rates are about 10 m s^{-1}. Zonal mean velocities are calculated using the sixth order polynomial profile from Sromovsky et al. (1993).

clouds (Smith et al. 1989). Since the companion clouds are within the same altitude range of clouds used to derive zonal wind profiles, it might be expected that they would drift at the mean zonal speed, but Table 5 shows that they do not. This can be explained by their dynamical connection to the dark vortex, which itself had a 20–30 m s^{-1} velocity offset from the zonal mean.

Measurement of companion cloud drift rates was done by manually tracking the center of light in individual images and dividing by image offset times to obtain velocities. For the 2016 and 2017 dark spot data, drift rates were determined by shifting longitudinal photometric profiles (as in Figure 2) using different rates, until the half-power points in the profiles were best aligned by eye. This method could not be used for the 2015.71 data, because SDS-2015 was positioned so close to the limb in some data frames that part of the vortex became indistinguishable from the surrounding atmosphere. To compensate for this effect, we manually determined the vortex position in each frame in the 2015.71 epoch, using WinJUPOS software.[17] For all measurements using the *HST* data, we estimate an uncertainty of about 10 m s^{-1}, including error contributions from image navigation uncertainty, noise in the image, and feature centroiding.

[17] WinJUPOS is available from http://jupos.org.

4. Discussion

4.1. Drifts and Oscillations

Dark vortices on Neptune have exhibited a range of meridional motions (Table 1), but SDS-2015 is the only one seen to drift poleward. Drift rates of SDS-2015 (Figure 4) are about an order of magnitude smaller than the equatorward drift rate of the GDS seen by *Voyager 2*, and two orders of magnitude smaller than the oscillatory drift of DS2 (Hammel et al. 1989; Sromovsky et al. 1993). Our observations cannot distinguish between several descriptions of the meridional motion of SDS-2015: poleward drift over the full 2015–2017 period, poleward drift from 2015 to 2016 followed by rest at 49°S, meandering, or poorly sampled oscillation. Latitudinal oscillation in the dark spot, if any, is not reflected in the behavior of bright companion clouds (Hueso et al. 2017), to within a precision of 1°.5, over the 2015 July–December period. The latitudinal stability of the companion clouds is robust, whether measurements are limited to large telescopes (*HST*, Keck, Lick, Calar Alto, Palomar) or combined with more frequently obtained amateur data. Most anticyclones in the vortex simulations of LeBeau & Dowling (1998) drifted equatorward, although some remained at a constant latitude and some experienced periods of poleward drift.

Longitudinal drift rates were measured separately for SDS-2015 and for its companion clouds (Table 5). At all epochs, the vortex system moved at a different rate compared to the zonal mean, and the companion clouds shared a common longitudinal drift rate with the dark spot.

Oscillations in shape were one of the most remarkable findings regarding the GDS (Smith et al. 1989). *Voyager* imaging sequences showed the GDS aspect ratio to vary by about a factor of 3 over a 290 hr period (assuming sinusoidal behavior). Table 4 lists aspect ratios for the shape of SDS-2015. The aspect ratio values lack the precision or temporal resolution that would be needed to demonstrate any oscillation in shape on such timescales. One significant limitation to determining the shape of the spot is set by the companion cloud, which locally reduces the photometric contrast needed to establish the dark spot boundary (Figure 1). A constant aspect ratio of 2 is consistent with the 2015–2017 measurements.

4.2. Implications for the Background Wind Field

As discussed in Section 1, Neptune's wind field may have complexities beyond the smooth *Voyager* profile of Sromovsky et al. (1993). The behavior and properties of SDS-2015 and its surroundings can provide insights into these complexities.

In the meridional direction, SDS-2015 originated in a dark band centered near −45° latitude, then drifted southward toward a bright band centered near −55°. No relationship between these bands and the zonal wind structure has ever been established. Albedo patterns are variable on decadal timescales at these latitudes. In 1989, *Voyager* found a broad dark band from 45° to 65°S (Smith et al. 1989). In 2003, *HST*/STIS observations instead found a narrower dark band centered at 60°S (Karkoschka & Tomasko 2011); the 45°–55°S range had grown bright. Twin dark bands are present in the 2015–2017 epoch, centered at 45°S and 60°S, with an intervening bright band at 51°S (Figure 1). To summarize, the dynamic area on Neptune is bounded near 65°S and 40°S in all three epochs, although the patterns of bright and dark between these bounds varied over time.

Jupiter has many alternating bright and dark bands, along with alternating eastward and westward jets. The jets are largely stable in position and magnitude, while coloration is variable and sometimes reverses (e.g., Rogers 1995; Fletcher et al. 2011; Tollefson et al. 2017b). Future research may determine whether any common processes operate on Neptune and Jupiter, where horizontal bands may remain stable in position, but be variable in color/brightness. Zonal winds on Jupiter seem to set up fixed boundaries for light and dark bands, although the winds cannot be the only control on coloration because band colors sometimes change even while winds remain stable. In Neptune's case, the smooth *Voyager* zonal wind profile provides no dynamical boundaries to constrain the dark bands evident in Figure 1, but there may be fine structure not currently resolved by the observations.

Vertical wind shear is expected to be present on Neptune, given the vertical and latitudinal variation in temperatures derived from *Voyager* data (Conrath et al. 1991; Fletcher et al. 2014). Observationally, the dispersion among zonal speeds of individual cloud tracers in ground-based imaging data (Fitzpatrick et al. 2014) may be a result of vertical wind shear. Dark vortices lie deeper in the atmosphere than other cloud tracers (Tollefson et al. 2017a), so their behavior may reveal differences between the deeper wind field and the zonal wind field based on *Voyager* observations of bright cloud tracers.

Although flow within the vortex cannot be directly measured, we can estimate the tangential velocity V of the vortex, based on assumptions regarding its vorticity. The spot resides in a latitude with anticyclonic vorticity. The relative vorticity $\zeta = du/dy = -3.4 \times 10^{-5}$ s^{-1} at the latitude of SDS-2015. The Coriolis parameter $f = -1.6 \times 10^{-4}$ s^{-1}, so the absolute vorticity $\zeta + f = -1.9 \times 10^{-4}$ s^{-1}. From Jupiter and Saturn we know that typically the intrinsic vorticity ζ_0 of vortices is halfway between ζ and f (Sromovsky et al. 1993; Legarreta and Sánchez-Lavega 2005; García-Melendo et al. 2007), so a rough estimate is $\zeta_0 = -10^{-4}$ s^{-1}. Defining for an elliptical circuit $\zeta_0 = VL_e/A$, where L_e is the length of the ellipse ($L_e = 2\pi a(1 - e^2/4 - O(e^4))$), e is the eccentricity, and $A = \pi ab$ is the area. Then,

$$V = \frac{b\zeta_0}{2(1 - e^2/4)} = -68 \text{ m s}^{-1}, \quad (2)$$

using $b = 1100$ km and $e = \sqrt{1 - b^2/a^2} = 0.87$ as typical values from Table 4.

Some time ago it was proposed that Neptune's dark spots could be Kida type vortices (Polvani et al. 1990). A stationary Kida vortex obeys the relationship

$$\zeta/\zeta_0 = \frac{1 - \lambda}{\lambda(1 + \lambda)}, \quad (3)$$

where $\lambda = b/a$ is the reciprocal aspect ratio. Taking $\lambda = 0.5$ as a representative value from Table 4, $\zeta/\zeta_0 = 0.67$ for a Kida vortex, which is greater than the value of $\zeta/\zeta_0 = 0.34$ derived above from the zonal flow and assumed intrinsic vorticity values.

The disagreement between these two estimates of ζ/ζ_0 may carry information regarding the deeper wind field to which the dark vortex may be sensitive. Specifically, our first estimate of ζ/ζ_0 relied on the value of $|du/dy|$ at the level of the cloud-tracked winds. But if SDS-2015 resides at a deep level where

$|du/dy|_{\rm deep} = 2 \times |du/dy|_{\rm Voy.}$, then the two methods for estimating ζ/ζ_0 would be exactly consistent.

4.3. The Demise of Dark Spots

An early goal of our observing program had been to check for equatorward drift of the vortex, in the hope of capturing widespread equatorial cloud activity resulting from the destruction of the vortex (LeBeau & Dowling 1998). The equatorward drift of the GDS may have ended in such an event, but there was no capability in 1990 to conduct observations with the sensitivity and resolution to detect it. The evolution of "Berg" on Uranus may have been an example of this mode of vortex demise (de Pater et al. 2011). If not for the annual cadence of OPAL observations, it might be thought that the eruption of widespread equatorial cloud activity in June–July 2017 (Molter et al. 2017) could potentially be related to the violent demise of SDS-2015.

But other dark spots did not seem to drift equatorward (Table 1). DS2 oscillated in latitude but had no known overall meridional drift; the end of this vortex was completely unconstrained. The northern vortices NDS-1994 and NDS-1996 appeared to have zero meridional drift (Sromovsky et al. 2001). These features eventually disappeared several years after discovery, but NDS-1994 curiously became invisible, while companion clouds at the same latitude remained for some time. The OPAL 2017 data show a persistent compact cloud at $-47\overset{\circ}{.}5$ latitude, nearly centered over a barely discernible dark spot with a much lower contrast than at the earlier times.

It seems that three out of the five known dark vortices (DS2, NDS-1994, and SDS-2015) are ending in the same way: with centered companion clouds. Companion clouds can make it harder to see the underlying vortex at blue wavelengths at *HST* resolution. At high resolution, *Voyager* images showed that unlike the GDS, DS2's companion clouds did not form at the periphery of the spot, but over the center. It would be interesting to model these data by degrading the *Voyager* images to *HST* resolution and assessing the effect of the centered companion clouds on the measured contrast of DS2.

The endings of NDS-1994 and NDS-1996 were not conclusively witnessed. Persistent cloud features remained at the latitude of NDS-1994, even after the dark vortex itself had ceased being directly visible. SDS-2017 may be following a similar evolutionary path. The companion clouds are centered, and the contrast of the dark spot is reduced to the point of being barely detectable.

4.4. Cadences for Planetary Observations

The importance of the time domain in observations of the planets in our solar system is now widely accepted. We are no longer in the era where the results of a flyby mission, or a single telescopic observation at a new wavelength (or with a higher spectral or spatial resolution) will automatically lead to major discoveries. But, discoveries remain to be made.

The OPAL program (Simon et al. 2015) represents a step into this new era. Approved by the STScI director as a discretionary program, this effort showed a commitment by a major astrophysical observatory to contribute to time-domain solar system science. The discovery of SDS-2015 is a direct result of that commitment. The discovery of dark vortices on Neptune is one example of science that has a timescale perfectly suited to OPAL's annual cadence of global map pairs.

Other observatories have contributed time-domain observations of the atmospheres of Neptune and other giant planets. *Kepler* K2 observations produced long-duration, short-cadence photometry (Simon et al. 2016). The resulting light curve data are valuable for comparison with brown dwarf and exoplanet variability, because the K2 Neptune observations were tied to resolved imaging data to interpret the simple photometric variation. A similar effort was done using *Spitzer* photometry (Stauffer et al. 2016). Twilight adaptive-optics imaging programs are building up a new campaign of frequent snapshot observations at Lick and Keck observatories (Molter et al. 2017), providing a higher-resolution complement to ground-based amateur coverage (Hueso et al. 2017).

Hypothetically, if OPAL 2017 observations had been too late to detect a small companion cloud centered over a very low-contrast dark spot, there would be a major open question: is the massive equatorial cloud activity in 2017 (Molter et al. 2017) related to the demise of SDS-2015? Proving such a link would require dense temporal sampling over throughout 2017, with 1000 km resolution, at visible blue wavelengths. Obtaining such coverage with the oversubscribed *HST* is very difficult, and a dedicated solar system space observatory is not yet available (Bell et al. 2015). Imaging with robotic visible-light adaptive optics, Robo-AO (Baranec et al. 2014), can fulfill the monitoring cadence and angular resolutions ($\sim 0\overset{''}{.}1$) required to measure the dynamics of major vortex and cloud activity on Neptune. A more capable Robo-AO system is being prepared for deployment on the UH 2.2 m telescope at Maunakea, HI, and part of its mission is to enable planetary science not feasible elsewhere.

Clearly, there is much room in the discovery space of solar system time domain science. There is room in this discovery space for exploration by a dedicated solar system space telescope, a network of ground facilities, and cadence programs at astrophysical observatories with advanced capabilities.

5. Summary

A new dark spot was discovered on Neptune in 2015 and observed through 2017. We draw the following conclusions and inferences:

1. The vortex drifted poleward, with a drift rate in the range of $1\overset{\circ}{.}7$–$2\overset{\circ}{.}5$/year (Figure 4).
2. The vortex faded over time (Figure 3), with a 467 nm contrast of $-6.6\% \pm 0.8\%$ in 2015.71 and $-2.9\% \pm 0.4\%$ in 2017.76. Bright companion clouds also grew increasingly centered over the dark spot with each successive observation (Figure 1). These evolutionary changes may be part of a vortex dissipation sequence, because aspects of these changes were seen in previous dark spots: DS2 had centered companion clouds during the *Voyager 2* encounter and was never seen again, and companion clouds of NDS-1994 persisted for some time after the dark spot itself faded from view.
3. If we make reasonable (but poorly constrained) assumptions about the vorticity of SDS-2015 and its surroundings (described in Section 4.2), then we find that the horizontal wind shear du/dy at the deep altitude of the vortex must be about twice the value measured by *Voyager* cloud-tracked winds.

4. Companion clouds create errors in measurements of the dark spot's boundaries, leading to uncertainties in the feature's size, shape, drift, and position that are large compared to other sources of error. Stated uncertainties in Table 4 include the effect of companion clouds on measurements of dark spot morphology.
5. Additional details of dark vortex behavior and evolution may be gleaned in the future, when faster cadence observations (with high spatial resolution at optical wavelengths) enable exploration of the time-domain discovery space.

Based on observations associated with programs GO-13937, GO-14044, GO-14334, GO-14492, and GO-14756, with support provided by NASA through grants from the Space Telescope Science Institute (operated by the Association of Universities for Research in Astronomy, Inc., under NASA contract NAS 5-26555). Data were obtained from the Data Archive at the Space Telescope Science Institute. Support was provided by the National Science Foundation through grant AST-1615004 and by the NASA Earth and Space Science Fellowship through grant NNX16AP12H to I.dP. and J.T., and by the Alfred P. Sloan Foundation and the National Science Foundation through grant AST-1712014 to C.B. We acknowledge support from grants AYA2015-65041-P (MINECO/FEDER, UE), Grupos Gobierno Vasco IT-765-13, and UPV/EHU UFI11/55 to A.S.L. and R.H.

We thank an anonymous reviewer for their quick and constructive review.

Facility: HST(WFC3).

Software: Astroconda, IDL, L.A.Cosmic, WinJUPOS, JPL Horizons Ephemerides.

ORCID iDs

Michael H. Wong https://orcid.org/0000-0003-2804-5086
Amy A. Simon https://orcid.org/0000-0003-4641-6186
Christoph Baranec https://orcid.org/0000-0002-1917-9157

References

Baranec, C., Riddle, R., Law, N. M., et al. 2014, ApJL, 790, L8
Bell, J. F., Schneider, N. M., Brown, M. E., et al. 2015, in LPI Contributions 1829, Kuiper: A Discovery-Class Observatory for Outer Solar System Giant Planets, Satellites, and Small Bodies, 6043
Conrath, B. J., Flasar, F. M., & Gierasch, P. J. 1991, JGR, 96, 18931
de Pater, I., Fletcher, L. N., Luszcz-Cook, S., et al. 2014, Icar, 237, 211
de Pater, I., Sromovsky, L. A., Hammel, H. B., et al. 2011, Icar, 215, 332
Deustua, S. E., Mack, J., Bajaj, V., & Khandrika, H. 2017, WFC3/UVIS Updated 2017 Chip-Dependent Inverse Sensitivity Values, Tech. rep., WFC3 ISR 2017-14 (Baltimore, MD: STScI)
Deustua, S. E., Mack, J., Bowers, A. S., et al. 2016, UVIS 2.0 Chip-dependent Inverse Sensitivity Values, Tech. rep., WFC3 ISR 2016-03 (Baltimore, MD: STScI), 3
Dressel, L. 2016, Wide Field Camera 3 Instrument Handbook, Version 8.0 (Baltimore, MD: STScI), http://documents.stsci.edu/hst/wfc3/documents/handbooks/cycle24/wfc3_cover.html
Fitzpatrick, P. J., de Pater, I., Luszcz-Cook, S., Wong, M. H., & Hammel, H. B. 2014, Ap&SS, 350, 65
Fletcher, L. N., de Pater, I., Orton, G. S., et al. 2014, Icar, 231, 146
Fletcher, L. N., Orton, G. S., Rogers, J. H., et al. 2011, Icar, 213, 564
Fruchter, A. S., & Hook, R. N. 2002, PASP, 114, 144
Fry, P. M., Sromovsky, L. A., de Pater, I., Hammel, H. B., & Rages, K. A. 2012, AJ, 143, 150
García-Melendo, E., Sánchez-Lavega, A., & Hueso, R. 2007, Icar, 191, 665
Hammel, H. B., Beebe, R. F., de Jong, E. M., et al. 1989, Sci, 245, 1367
Hammel, H. B., & Lockwood, G. W. 1997, Icar, 129, 466
Hammel, H. B., Lockwood, G. W., Mills, J. R., & Barnet, C. D. 1995, Sci, 268, 1740
Hammel, H. B., Sromovsky, L. A., Fry, P. M., et al. 2009, Icar, 201, 257
Hueso, R., de Pater, I., Simon, A., et al. 2017, Icar, 295, 89
Ingersoll, A. P., Dowling, T. E., Gierasch, P. J., et al. 2007, in Jupiter, ed. F. Bagenal, T. E. Dowling, & W. B. McKinnon (Cambridge: Cambridge Univ. Press), 105
Irwin, P. G. J., Wong, M. H., Simon, A. A., Orton, G. S., & Toledo, D. 2017, Icar, 288, 99
Karkoschka, E. 2011, Icar, 215, 759
Karkoschka, E., & Tomasko, M. G. 2011, Icar, 211, 780
LeBeau, R. P., & Dowling, T. E. 1998, Icar, 132, 239
Legarreta, J., & Sánchez-Lavega, A. 2005, Icar, 174, 178
Lii, P. S., Wong, M. H., & de Pater, I. 2010, Icar, 209, 591
Limaye, S. S., & Sromovsky, L. A. 1991, JGR, 96, 18941
Mack, J., Dahlen, T., Sabbi, E., & Bowers, A. S. 2016, Chip-Dependent Flats, Tech. rep., WFC3 ISR 2016-04 (Baltimore, MD: STScI), 4
Martin, S. C., de Pater, I., & Marcus, P. 2012, Ap&SS, 337, 65
Minnaert, M. 1941, ApJ, 93, 403
Molter, E. M., de Pater, I., Alvarez, C., Tollefson, J., & Luszcz-Cook, S. H. 2017, in AGU Fall Meeting Abstracts, P31D-2856
Polvani, L. M., Wisdom, J., Dejong, E., & Ingersoll, A. P. 1990, Sci, 249, 1393
Rogers, J. H. 1995, The Giant Planet Jupiter (Cambridge: Cambridge Univ. Press)
Sánchez-Lavega, A., Sromovsky, L., Showman, A., et al. 2018, in Zonal Jets, ed. P. Galperin & B. Read (Cambridge: Cambridge Univ. Press)
Shetty, S., & Marcus, P. S. 2010, Icar, 210, 182
Simon, A. A., Rowe, J. F., Gaulme, P., et al. 2016, ApJ, 817, 162
Simon, A. A., Wong, M. H., & Orton, G. S. 2015, ApJ, 812, 55
Simon, A. A., Wong, M. H., Rogers, J. H., et al. 2014, ApJL, 797, L31
Smith, B. A., Soderblom, L. A., Banfield, D., et al. 1989, Sci, 246, 1422
Sromovsky, L. A., de Pater, I., Fry, P. M., Hammel, H. B., & Marcus, P. 2015, Icar, 258, 192
Sromovsky, L. A., Fry, P. M., & Baines, K. H. 2002, Icar, 156, 16
Sromovsky, L. A., Fry, P. M., Dowling, T. E., Baines, K. H., & Limaye, S. S. 2001, Icar, 149, 459
Sromovsky, L. A., Limaye, S. S., & Fry, P. M. 1993, Icar, 105, 110
Sromovsky, L. A., Limaye, S. S., & Fry, P. M. 1995, Icar, 118, 25
Stauffer, J., Marley, M. S., Gizis, J. E., et al. 2016, AJ, 152, 142
Stratman, P. W., Showman, A. P., Dowling, T. E., & Sromovsky, L. A. 2001, Icar, 151, 275
Tollefson, J., de Pater, I., Marcus, P. S., et al. 2018, Icar, submitted
Tollefson, J., Luszcz-Cook, S. H., Wong, M. H., & de Pater, I. 2017a, in AAS/DPS Meeting 49 Abstracts, 205.03
Tollefson, J., Wong, M. H., de Pater, I., et al. 2017b, Icar, 296, 163
van Dokkum, P. G. 2001, PASP, 113, 1420
Wong, M. H. 2010, Amplitude of fringing in WFC3/UVIS narrowband red filters, Tech. rep., WFC3 ISR 2010-04 (Baltimore, MD: STScI), 4
Wong, M. H. 2011, in Proc. 2010 Space Telescope Science Institute Calibration Workshop, ed. S. Deustua & C. Oliveira (Baltimore, MD: STScI), 22
Wong, M. H., Fry, P. M., & Simon, A. A. 2016, CBET, 4278, http://www.cbat.eps.harvard.edu/cbet/004200/CBET004278.txt